Microseismic joint location and anisotropic velocity inversion for hydraulic fracturing in a tight Bakken reservoir

GEOPHYSICS, VOL. 79, NO. 5 (SEPTEMBER-OCTOBER 2014); P. C111–C122, 16 FIGS., 1 TABLE.
10.1190/GEO2013-0345.1

Microseismic joint location and anisotropic velocity inversion for hydraulic fracturing in a tight Bakken reservoir

Junlun Li[1], Chang Li[2], Scott A. Morton[2], Ted Dohmen[2], Keith Katahara[2], and M. Nafi Toksöz[1]

ABSTRACT

To improve the accuracy of microseismic event locations, we developed a new inversion method with double-difference constraints for determining the hypocenters and the anisotropic velocity model for unconventional reservoirs. We applied this method to a microseismic data set monitoring a Middle Bakken completion in the Beaver Lodge area of North Dakota. Geophone arrays in four observation wells improved the ray coverage for the velocity inversion. Using an accurate anisotropic velocity model is important to correctly assess the height growth of the hydraulically induced fractures in the Middle Bakken. Our results showed that (1) moderate-to-strong anisotropy exists in all studied sedimentary layers, especially in the Upper and Lower Bakken shale formations, where the Thomsen parameters (ϵ and γ) can be greater than 0.4, (2) all the events selected for high signal-to-noise ratio and used for the joint velocity inversion are located in the Bakken and overlying Lodgepole formations, i.e., no events are detected in the Three Forks formation below the Bakken, and (3) more than half of the strong events are in two clusters at approximately 100 and 150 m above the Middle Bakken. Reoccurrence of strong, closely clustered events suggested activation of natural fractures or faults in the Lodgepole formation. The sensitivity analysis for the inversion results showed that the relative uncertainty in parameter δ is larger than other anisotropy parameters. The microseismic event locations and the anisotropic velocity model are validated by comparing synthetic and observed seismic waveforms and by S-wave splitting.

INTRODUCTION

Given their extremely low matrix permeability, gas- or oil-bearing tight sandstones require successfully engineered fracture networks that generate flow paths for economical oil and gas production. Depending on the geology, local stress regime, petrology, heterogeneities, and pumping rates, the hydraulically fractured networks can vary significantly from one place to another. Therefore, mapping of the fractures is a crucial input for production and for designing fracturing operations, especially in areas where few such activities have been performed before. Microseismic monitoring has been used for more than a decade to map hydrofracture networks during well completions (e.g., Rutledge and Phillips, 2003; Maxwell et al., 2010). However, there are inherent uncertainties in locating microseismic events. These uncertainties come from several sources: (1) limited geometry of monitoring arrays, (2) phase picking errors, especially for events with a low signal-to-noise ratio (S/N), (3) downhole geophone orientations that are often not well constrained, and (4) inaccuracy in velocity models constructed from well logs or perforation shots (e.g., Warpinski et al., 2005), especially when strong anisotropy exists (Warpinski et al., 2009). In addition, if the microseismic events occur far from the perforation shots, the calibrated velocity models from perforation shots may not be truly representative (e.g., Rutledge and Phillips, 2003; Warpinski et al., 2008). To deal with the anisotropy issue, Grechka et al. (2011) propose a method to estimate effective anisotropy simultaneously with locations of microseismic events in a homogeneous medium.

In our previous studies (Li et al., 2012b, 2013), we derived the analytical sensitivities and the inversion scheme for the simultaneous double-difference location and anisotropic layered velocity inversion problem. In this study, we apply this method to a Bakken microseismic data set monitored at four wells. Besides providing coverage for detecting microseismic events along a long lateral

Manuscript received by the Editor 12 September 2013; revised manuscript received 24 February 2014; published online 21 July 2014.
[1]Massachusetts Institute of Technology, Earth Resources Laboratory, Department of Earth, Atmospheric, and Planetary Sciences, Cambridge, Massachusetts, USA. E-mail: junlunli@mit.edu; toksoz@mit.edu.
[2]Hess Corporation, Houston, Texas, USA. E-mail: chang.li@chevron.com; smorton@hess.com; tdohmen@hess.com; kkatahara@hess.com.

well, multiple monitoring wells help to improve the ray coverage, providing better constraints for the velocity inversion. We validate the microseismic event locations and anisotropic velocity models by comparing synthetic and observed seismic waveforms. Observed S-wave splitting also supports the determined anisotropy values. By using an accurate anisotropic velocity model, one can better locate events, helping constrain the dimensions of the induced fractures, especially their height.

GEOLOGY OF THE STUDIED FORMATIONS

The Bakken formation was deposited during the lowermost Mississippian period and is a relatively thin unit limited in areal extent to the deeper part of the Williston Basin. Organic-rich shales in the Bakken have been documented as excellent source rocks for the petroleum found in reservoirs located around the unit (Meissner, 1991). Our monitoring site is located in the Beaver Lodge area of North Dakota. In this area, the Bakken is further divided into three members, namely an upper shale member, a middle siltstone member, and a lower shale member, with a total thickness of approximately 36.5 m (120 ft). Oil production comes primarily from the Middle Bakken. The Bakken formation is conformably overlain by the Lodgepole formation deposited during the Mississippian period, and the lowermost Lodgepole formation, adjacent to the Bakken, consists primarily of interbedded lime mudstones and calcareous shales. The Bakken formation unconformably overlies the Three Forks formation deposited during the Upper Devonian period, which consists primarily of interbedded, highly dolomitic, siltstones, and shales.

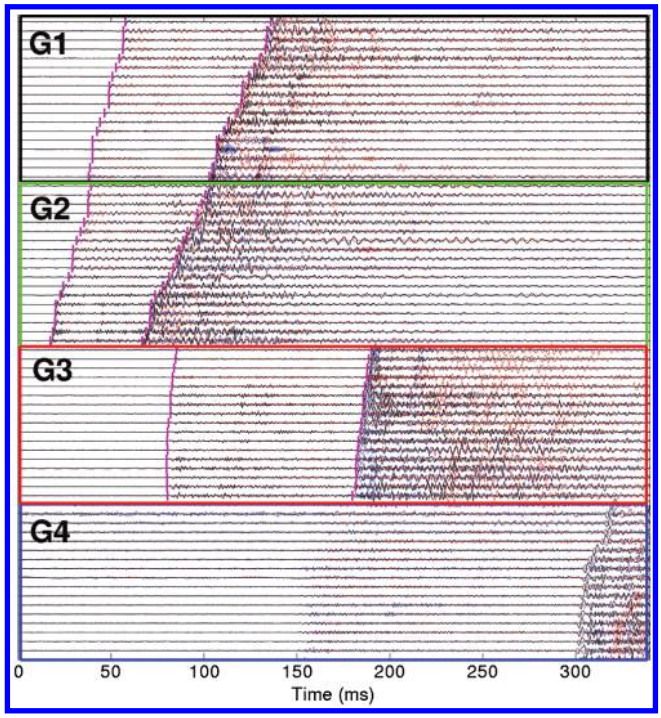

Figure 1. Seismic waveforms recorded by 3C geophones in G1, G2, G3, and G4 from a strong event in cluster 2 (see Figure 3). The magenta lines represent the P- and SH-wave picks. Traces from two horizontal components and one vertical component are overlaid with different colors (black, blue, and red). Due to large distance (>1 km) and low S/Ns in array G4, only picks from G1, G2, and G3 were used for velocity inversion and the location of this event.

MICROSEISMIC DATA SET AND PREVIOUS RESULTS

In May 2010, Hess Corporation conducted a microseismic survey over a two-day period in the Beaver Lodge area of North Dakota (Hayles et al., 2011). The treatment was in a 3050-m Bakken horizontal well. Two producing wells and two injection wells were used as monitoring wells with 17 or 18 3C geophones in each well. The microseismic data were sampled at 0.25 ms over the monitoring period. This is an entirely sliding-sleeve completion, so no perforation shot was performed, and the geophone orientations were calibrated with string shots in the four monitoring wells.

This microseismic data set was processed by four different vendors (Hayles et al., 2011). Each vendor constructed its own velocity model calibrated by the string shots, ball setting events, well logs, and VSP information. These vendors differ in terms of the information they used in processing the data set. One vendor used the P- and S-wave arrivals and the hodograms from a single well, whereas another vendor used a diffraction stacking technique on P-wave recorded on all available monitoring wells. As a result of differences in phase picks, velocity models, location methods, etc., the microseismic locations provided by these vendors vary considerably. The inconsistency in event locations hindered estimates of stimulated reservoir volume (SRV) and evaluation of the fracture height growth. Li et al. (2012a) show that one vendor's results are more consistent with the raw microseismic data using each vendor's velocity model and event locations and comparing predicted arrival times with the actual picks. However, because there are no perforation shots in this survey, uncertainties in the calibrated velocity models are considerable even in the best vendor's results. In the following, we will show an improvement in microseismic event location by joint anisotropic velocity inversion.

PREPROCESSING AND METHODOLOGY

Raw microseismic data processing

Over the monitoring period of two days, several hundred microseismic events were detected. To give more even distribution of events for velocity inversion and to avoid the greater picking errors for low S/N events, we selected several strong events in each fracturing stage and created a database of 100 events from all 16 completion stages. Most of these 100 events were recorded by more than one monitoring well. Due to strong anisotropy in this region (Hayles et al., 2011), the SV-waves often arrive appreciably later than the SH-waves and are contaminated by SH coda and other converted waves. Therefore, due to larger uncertainties in picked SV-wave arrivals, we used only the P- and SH-wave arrivals for location and velocity inversion. Although Grechka et al. (2011) show that the anisotropic parameters can be characterized by including all P-, SH-, and SV-wave arrivals, Li et al. (2013) in their theoretical study and synthetic tests also find that the parameters can still be determined if only P- and SH-wave arrivals are used. After careful quality-control on arrival picks, we selected 68 events with the best S/Ns for the anisotropic velocity inversion. Figure 1 shows the seismograms and the picks for a strong event that was observed by all four monitoring wells. For this event, only picks from wells G1, G2,

and G3 were used for location and velocity inversion due to exceedingly large epicentral distance (>1 km) and low S/Ns for well G4 (distribution of wells shown in Figure 2).

Because the azimuthal coverage of a downhole monitoring survey is generally poor, and thus locating the event with traveltime information alone is often unreliable, the back azimuths for the P-waves are used to help locate the events. The back azimuths are determined by analyzing the eigenvector of the dominant eigenvalue of the seismic trace covariance matrices or hodograms (Magotra et al., 1989). Dreger et al. (1998) find that including back azimuths can improve the event locations when the stations are deployed in a narrow azimuthal range related to the events. For this data set, we noted that back azimuths may be subject to appreciable uncertainty because we only have string shots to constrain the geophone orientations. Therefore, we used the P-wave back azimuths to constrain the event locations but gave them less weight.

Initial VTI velocity model

We assumed a vertical transverse isotropy (VTI) model for the following reasons. In this part of the Bakken, structural dip is small. It reaches 2° in spots, but is well below 1° over most of the study area. Crossed dipole logs in vertical wells show little evidence for azimuthal anisotropy. Surface seismic data over this field have not been processed for azimuthal anisotropy. However, moveout velocity and amplitude-variation-with-offset behavior show small azimuthal variations in a neighboring area with similar geology. The azimuthal anisotropy in the neighboring area is relatively small compared with the VTI anisotropy. We have assumed that our area behaves similarly.

To construct a starting model, we first divided the section into layers each with almost homogeneous velocity, using well logs from the observation wells to determine thicknesses of the layers. Then, we computed average properties for each stratigraphic layer using sonic logs from a vertical Bakken well in this area. The available sonic properties in that well were vertical V_P and V_S, and Thomsen parameter γ (Thomsen, 1986). Parameter γ was estimated by combining shear velocities from dipole and Stoneley modes (e.g., Tang, 2003; Walsh et al., 2007). The vertically propagating S-waves showed negligible splitting, consistent with VTI symmetry. We then assumed $\epsilon = \gamma$, roughly consistent with other observations (Horne, 2013). Finally, we assumed $\delta = 0.5\epsilon$, which lies within the large scatter in observations (Vernik and Liu, 1997; Havens, 2012; Horne, 2013). In fact, Thomsen's δ is poorly constrained by well data. These parameters and relations are only used as references in our inversion, i.e., they are allowed to change slightly with iteration.

Inversion method

In our study, we constrain the velocity structure as a 1D layered VTI medium and invert for the density-normalized elastic moduli C_{ij}^k and thickness L_k for each layer k, as well as the hypocenters and origin times of all events. The analytic sensitivities were derived for these parameters, and for brevity, the derivations are not repeated in this paper (Li et al., 2012b, 2013). To forward model the traveltimes, we used the generalized Snell's law for tracing rays in a VTI layered medium analytically with asymptotic high-frequency approximation (Tang and Li, 2008). Extensive tests using synthetic data validate our method.

To improve the relative locations of the events, we use a double-difference velocity inversion method where the differential traveltimes and differential back azimuths are used. Let us denote the observed arrival time from event i to station k as ${}^o t_k^i$, and the modeled one as ${}^m t_k^i$. The arrival time data residual can be expressed as

$$ {}^t r_k^i = {}^o t_k^i - {}^m t_k^i = \sum_{l=1}^{3} \frac{\partial T_k^i}{\partial x_l^i} \Delta x_l^i + \Delta \tau^i, \tag{1} $$

where $x_l \in \{x_s, y_s, z_s\}$ is the hypocenter, T is the traveltime, and τ is the origin time; Δx and $\Delta \tau$ are corrections to the hypocenter and the origin time determined from data residuals ${}^t r$. We take the difference between the arrival time residuals from event pairs i and j to a common station k, it becomes the double-difference location method first proposed by Waldhauser and Ellsworth (2000) as follows:

$$ {}^t r_k^i - {}^t r_k^j = \sum_{l=1}^{3} \frac{\partial T_k^i}{\partial x_l^i} \Delta x_l^i + \Delta \tau^i - \sum_{l=1}^{3} \frac{\partial T_k^j}{\partial x_l^j} \Delta x_l^j - \Delta \tau^j, \tag{2} $$

where

$$ {}^t r_k^i - {}^t r_k^j = (t_k^i - t_k^j)^o - (t_k^i - t_k^j)^m. \tag{3} $$

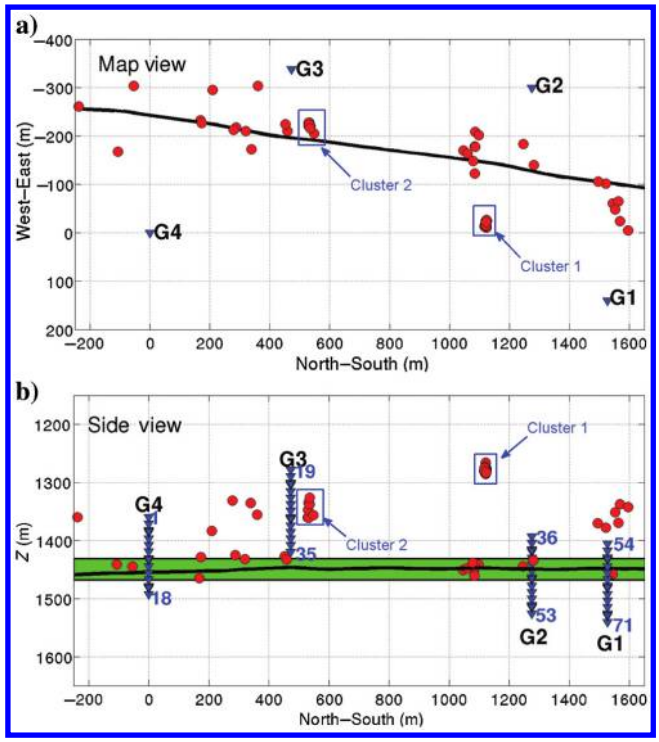

Figure 2. The microseismic event locations from the anisotropic velocity inversion in the map view (a) and side view (b). The blue triangles represent the four arrays (G1, G2, G3, and G4), and the blue numbers are the geophone IDs used for later discussion. Note the geophone sequence starts from the top to the bottom of well G4, then followed by wells G3, G2, and G1. The black line indicates the portion of the horizontal well path in the Middle Bakken. The green shadow region indicates the Bakken formation. The red dots represent the determined locations of the 68 selected strong events. The two blue boxes denote the locations of two groups of clustered events in the Lodgepole.

The double-difference method is capable of eliminating the unmodeled common error existing on the closely spaced raypaths from a cluster of events to a receiver (Zhang and Thurber, 2003, 2006). In our inversion, the differential times are obtained from waveform crosscorrelation. Note the differential criterion is automatically applied only to events pairs with hypocentral distance less than 30 m to assure the raypaths are similar.

Similar to the double-difference for traveltimes, we can extend this method for back azimuths. First, the residual for a back azimuth observation can be expressed as

$$ {}^{\varphi}r_k^i = \sum_{l=1}^{3} \frac{\partial \varphi_k^i}{\partial x_l^i} \Delta x_l^i, \tag{4}$$

where ${}^{\varphi}r$ is the back azimuth residual. And the corresponding double-difference form is

$$ {}^{\varphi}r_k^i - {}^{\varphi}r_k^j = \sum_{l=1}^{3} \frac{\partial \varphi_k^i}{\partial x_l^i} \Delta x_l^i - \sum_{l=1}^{3} \frac{\partial \varphi_k^j}{\partial x_l^j} \Delta x_l^j. \tag{5}$$

The inversion scheme for determining the velocity structure and the hypocenters can be written in the following form:

$$ \begin{bmatrix} \mathbf{Q}_{\mathbf{DD}}^{\mathbf{t}}\mathbf{A}^{\mathbf{t}} \\ \mathbf{Q}_{\mathbf{DD}}^{\boldsymbol{\varphi}}\mathbf{A}^{\boldsymbol{\varphi}} \\ w^t\mathbf{A}^{\mathbf{t}} \\ w^{\varphi}\mathbf{A}^{\boldsymbol{\varphi}} \\ w^c\mathbf{P}^{\mathbf{c}} \end{bmatrix} \begin{bmatrix} \boldsymbol{\Delta}\mathbf{C}_{\mathbf{ij}} \\ \boldsymbol{\Delta}\mathbf{L} \\ \boldsymbol{\Delta}\mathbf{X} \end{bmatrix} = \begin{bmatrix} \mathbf{Q}_{\mathbf{DD}}^{\mathbf{t}}\boldsymbol{\Delta}\mathbf{T} \\ \mathbf{Q}_{\mathbf{DD}}^{\boldsymbol{\varphi}}\boldsymbol{\Delta}\boldsymbol{\varphi} \\ w^t\boldsymbol{\Delta}\mathbf{T} \\ w^{\varphi}\boldsymbol{\Delta}\boldsymbol{\varphi} \\ -w^c\mathbf{P}^{\mathbf{c}}\mathbf{C}_{\mathbf{ij}}^{\mathbf{0}} \end{bmatrix}, \tag{6}$$

where $\mathbf{Q}_{\mathbf{DD}}^{\mathbf{t}}$ and $\mathbf{Q}_{\mathbf{DD}}^{\boldsymbol{\varphi}}$ are the differential matrices for traveltimes (Wolfe, 2002; Zhang and Thurber, 2006) and back azimuths, respectively; w^t and w^{φ} are the relative weights for absolute traveltimes and back azimuths, respectively; $\mathbf{A}^{\mathbf{t}} = [\mathbf{M}^{\mathbf{t}} \quad \mathbf{H}^{\mathbf{t}}]$ is the sensitivity matrix of the traveltime with respect to the velocity structure ($\mathbf{M}^{\mathbf{t}}$), and the event hypocenter ($\mathbf{H}^{\mathbf{t}}$); $\mathbf{A}^{\boldsymbol{\varphi}} = [\mathbf{0} \quad \mathbf{A}^{\boldsymbol{\varphi}}]$ is the sensitivity matrix of the back azimuth with respect to the hypocenter; $\mathbf{P}^{\mathbf{c}}$ is the constraint operator on the density normalized elastic moduli $\mathbf{C}_{\mathbf{ij}}$ that attempts to retain some predetermined anisotropic parameters ϵ, δ or γ estimated from the well logs. Note that the weight w^c controls how much the Thomsen's parameters or the ratios among different elastic moduli can change with iteration. A detailed discussion of the operator P^c can be found in Appendix D in Li et al. (2013). The expression $\boldsymbol{\Delta}\mathbf{C}_{\mathbf{ij}}$ is the perturbation on the density normalized elastic moduli; $\boldsymbol{\Delta}\mathbf{L}$ is the perturbation on the layer thickness; $\boldsymbol{\Delta}\mathbf{X}$ is the perturbation on the hypocenter and origin time of events; $\boldsymbol{\Delta}\mathbf{T}$ is the traveltime residual; and $\boldsymbol{\Delta}\boldsymbol{\varphi}$ is the back azimuth residual. Following the strategy by Zhang and Thurber (2006) and Zhang et al. (2009), we use larger w^t and w^{φ} in the beginning, and we gradually decrease these weights with iteration. This dynamic weighting approach first determines the absolute event locations and the velocity model, as the layered velocity structure is only sensitive to the absolute information (Li et al., 2013), then improves the event relative locations by gradually emphasizing the relative information.

In our inversion, we parameterize the density normalized elastic moduli with the unit of GPa $\times$ cm^3/g because we found such parameterization would make the sensitivity more balanced for elastic moduli, layer thicknesses (meter), and source parameters (meter for hypocenter, second for origin time). Note, here the elastic moduli are density-normalized, but for simplicity we still use $\mathbf{C}_{\mathbf{ij}}$ in the equations (e.g., Grechka et al., 2011). The Levenberg-Marquardt algorithm (Levenberg, 1944) is used for the inversion. The nonlinear inverse problem involving the velocity structure and the event parameters is linearized and solved with iterations. In each iteration, the parameters are corrected with $\boldsymbol{\Delta}\mathbf{C}_{\mathbf{ij}}$, $\boldsymbol{\Delta}\mathbf{L}$, and $\boldsymbol{\Delta}\mathbf{X}$, respectively. We iterate the inversion until the reduction in residuals becomes negligible. Usually, 15 iterations are required. It should be noted that the elastic moduli for the VTI medium can also be parameterized with Thomsen's notation in the velocity inversion (e.g., Zhou and Greenhalgh, 2005a, 2007, 2008).

INVERTED MICROSEISMIC EVENT LOCATIONS AND ANISOTROPIC PARAMETERS

We first used the best vendor's layered isotropic velocity models, one for each well, to locate 100 selected events with a global search method (e.g., Zhang et al., 2009) for hypocenters and origin times that minimizes the traveltimes and the back azimuth information. The determined values from the global search are then used as the initial guess for further study. Eventually, 68 out of the 100 selected events with most confident picks are used for the joint anisotropic velocity inversion and double-difference event location.

For the anisotropic velocity inversion, we start with the layered VTI velocity model described earlier. Using the phase and group velocity relations in the VTI medium together with the generalized Snell's law to account for refraction at the interfaces (Tang and Li, 2008), we traced rays in the layered VTI medium and calculated traveltimes and back azimuths, as well as all the sensitivities in equation 6 analytically (Li et al., 2012b, 2013). We then inverted for the anisotropic velocity and the thickness of each layer as well as for hypocenters of the 68 selected strong events. As the layer interfaces are well characterized by well logs, we put heavy damping on the layer thicknesses in the inversion and thus the thicknesses changed only slightly.

Figure 2 shows the map and side views of the determined locations of the 68 selected strong microseismic events. All these events are located within the Bakken and Lodgepole formations, and no strong events are located beneath the Bakken formation. Also, more than half of the selected events are located in two clusters at approximately 150 and 100 m above the Bakken, respectively.

Figure 3 shows the final inverted six-layer anisotropic (VTI) model for the Lodgepole, the Bakken and the Three Forks formations (Table 1). The anisotropy of the Upper and Lower Bakken shale is quite strong, with Thomsen's ϵ and γ being greater than 0.4. Table 1 shows the initial and final vertical V_P and V_S as well as the Thomsen's parameters ϵ, δ, and γ, which are converted from the inverted density normalized elastic moduli $\mathbf{C}_{\mathbf{ij}}$ (Thomsen, 1986). The changes in vertical velocities relative to the starting model are less than 7% for all layers, and the changes for Thomsen parameters can be larger than 10%, especially for those parameters with very small values. As mentioned before, the initial values of the Thomsen parameters come with varying confidence from the well logs, and, therefore, we allow some degree of alteration in the inversion with constraints. We address uncertainties and sensitivities due to varying ray coverage later in this paper. It also should be pointed out, as Li et al. (2012b, 2013) discussed, that the differential information does not improve the inversion for the layered VTI structure

but only the relative locations of the events in our case. This is because we do not parameterize the source regions into small cells for 3D heterogeneous tomography (Zhang and Thurber, 2006). In that case, the differential traveltimes would be sensitive to the structure close to the neighboring events.

Dense-ray coverage is the key for a successful inversion result. Figures 4 and 5 show the P- and SH-raypaths used for the anisotropic velocity inversion, respectively. From the side views, we can see clearly that multiple monitoring wells at varying distances help to improve the ray angle coverage, thereby providing better constraints on the anisotropic parameters for the VTI velocity inversion. Figures 4 and 5 also show that ray angle coverage varies noticeably in different layers, and the lengths of raypaths and corresponding traveltimes in each layer also change significantly, indicating different parameters in different layers are inverted with varying degrees of certainty. In Appendix A, we perform a thorough analysis of the uncertainties for the inverted parameters.

Figure 6 shows the comparison between the synthetic and observed P-wave and SH-wave traveltimes (upper) and their residuals (lower) for the 68 selected strong events after the anisotropic velocity inversion with double-difference relocation. The traveltime residual for P- and SH-waves has a standard deviation of 0.9 and 1.2 ms, respectively; both have near-zero mean. These standard deviations are much smaller than those of the previously reported best vendor result in this data set, which is 4.85 ms (Li et al., 2012a). Still, the residuals at some receivers from a few events within the Bakken formation are larger than the rest. These anomalous residuals are likely due to inaccurate picking of the unclear first arrivals caused by multiple refractions and reflections of the waves among the closely spaced Bakken members. Other than these few cases, we did not find traveltime residuals of different events have any distinct spatial distribution. That is, the events located in the northern part

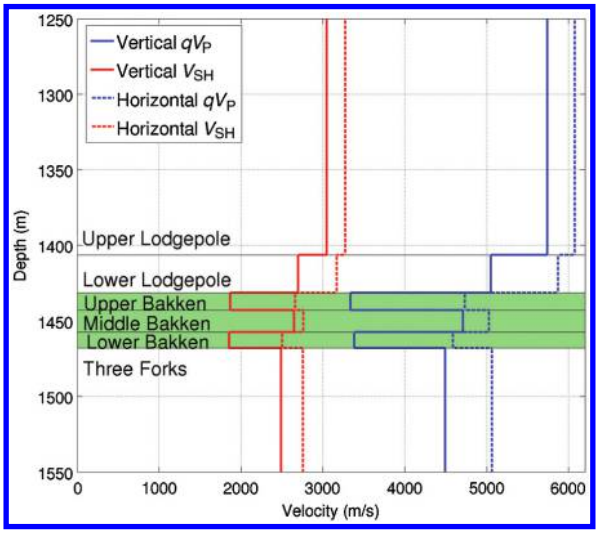

Figure 3. Final layered anisotropic (VTI) velocity model obtained from the joint anisotropic velocity inversion. The vertical axis is the depth relative to a datum in meters. The blue and red lines are P- and S-wave velocities, respectively. The solid and dashed lines are the vertical and horizontal velocities, respectively. The green shadow zone indicates the Bakken formation.

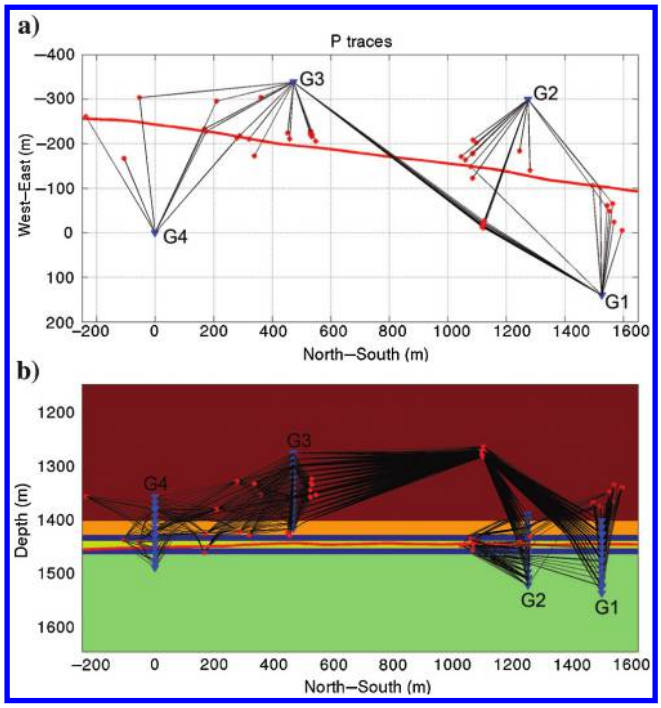

Figure 4. The ray coverage of P-waves for the anisotropic velocity inversion in the map view (a) and side view (b). The raypaths from the located events (red stars) to each geophone (blue triangles) are shown with black lines. The bold red line shows the horizontal treatment well path in the Middle Bakken. The background colors indicate the vertical P-wave velocities as shown in Figure 3.

Table 1. Comparison between the initial and inverted anisotropic parameters. Here, V_P and V_S are the vertical P- and S-wave velocities, respectively.

	Initial model					Inverted model				
VTI parameters	V_P (m/s)	V_S (m/s)	ϵ	δ	γ	V_P (m/s)	V_S (m/s)	ϵ	δ	γ
Upper Lodgepole	5776	3144	0.057	0.028	0.057	5739	3047	0.060	0.021	0.077
Lower Lodgepole	5215	2823	0.167	0.084	0.167	5052	2701	0.175	0.074	0.188
Upper Bakken	3157	1823	0.487	0.243	0.487	3338	1868	0.506	0.236	0.516
Middle Bakken	4766	2797	0.059	0.029	0.059	4710	2649	0.069	0.014	0.044
Lower Bakken	3303	1889	0.386	0.193	0.386	3381	1858	0.421	0.139	0.409
Three Forks	4667	2627	0.120	0.060	0.120	4493	2490	0.135	0.037	0.112

(larger observation numbers for P and SH) do not have statistically different residuals than the events from the southern part. Nor did we find the traveltime residuals have noticeable azimuthal distribution associated with fracture-induced HTI anisotropy (Zhou and Greenhalgh, 2005b, 2006). The consistent residual distribution means our inverted anisotropic velocity model is appropriate for the whole region of interest. It should be noted that if reflected and converted phases can be correctly identified in the wave trains, they can be used to further constrain the velocity inversion (e.g., Huang et al., 2012; Bai et al., 2013). However, for this data set, the reflected and converted phases were practically used and were largely dominated by scattered waves from heterogeneities and fractures. Figure 7 shows the comparison between the synthetic and observed back azimuths. The mean of the residual is 2.8°, and the standard deviation of the residual is 8°. One might expect a bit smaller residual considering most of the events are of good quality, but the lack of perforation shots makes the orientations of our geophones less certain.

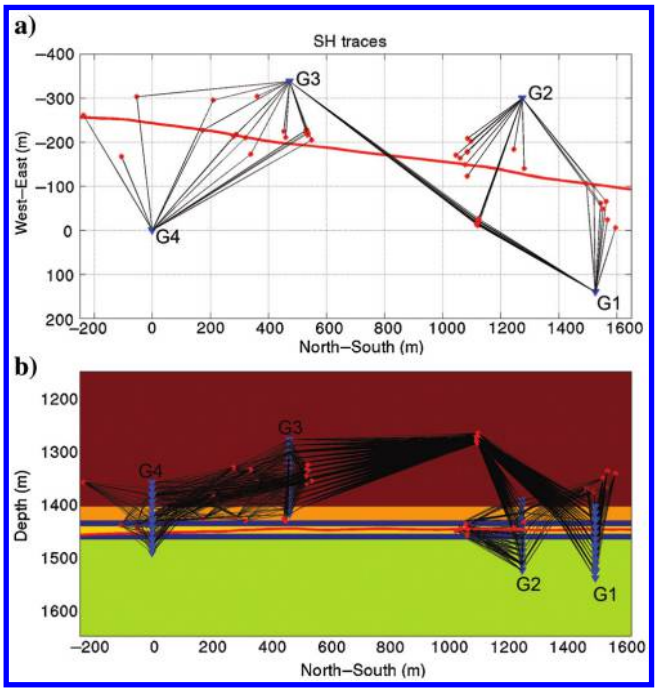

Figure 5. Same with Figure 4, but for SH-waves. The background colors indicate the vertical S-wave velocities as shown in Figure 3.

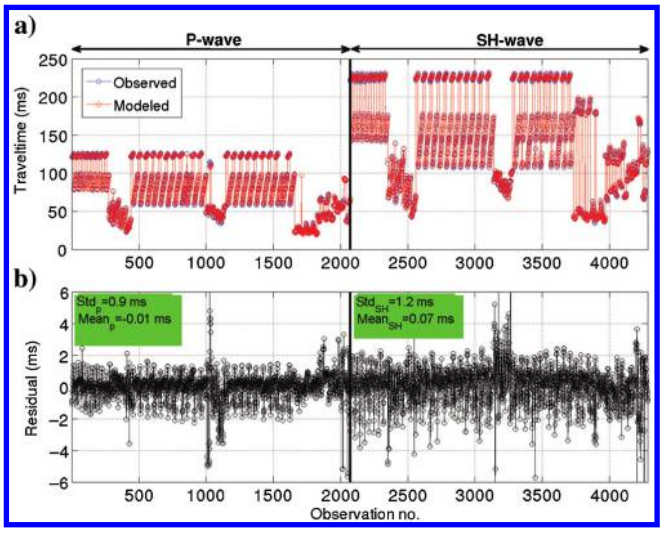

Figure 6. Comparison between the synthetic and observed P- and SH-wave arrivals (a) and their residuals (b). To the left of the bold black line are the P-wave traveltimes for the 68 events used for the anisotropic velocity inversion, and to the right are the SH-wave traveltimes. The traveltimes are first ordered according to the observation type (P or SH) and then according to the event ID; for each event, the traveltimes are ordered according to the receiver number (Figure 2). Most of the residuals are approximately 1% or less of the total traveltimes.

DISCUSSION

Clustered events

Among the 68 strong events, more than half are located approximately 100–150 m above the treatment well in the Bakken. We note that 29 events from several different completion stages are closely clustered within a tiny space — less than 20 m in diameter (cluster 1 in Figure 2). These events are among the strongest selected events, and most are detected by three monitoring wells. Castellanos and Van der Baan (2013) and Kocon and Van der Baan (2012) find that event groups with highly correlated waveforms known as multiplets can illuminate the time picks and event location quality. Figure 8a shows P-waveform comparisons for the 29 events in cluster 1 at a receiver in well G1. Except for a few events, the crosscorrelation coefficients (normalized to unity) for event pairs are greater than 0.7, indicating that the hypocenters and the source properties are similar. The reoccurrence of events in the same location is well-known in earthquake seismology and usually implies reactivation of a fault (e.g., Li et al., 2011). Thus, the close clustering of these 29 big events from different stages at approximately 150 m above the treatment well suggests that a natural fracture swarm or a fault zone is being repeatedly activated due to injection of pressurized fluids during some of the completions. Figure 8b

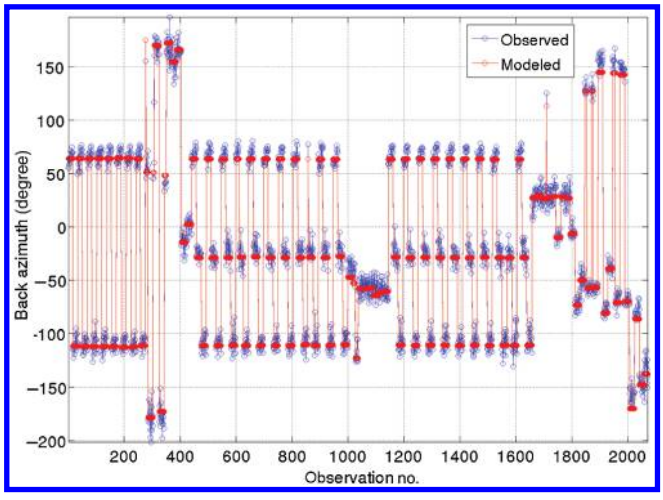

Figure 7. Comparison between the synthetic and observed back azimuths for the P-waves. The mean and standard deviation of the residuals are 2.8° and 8°, respectively.

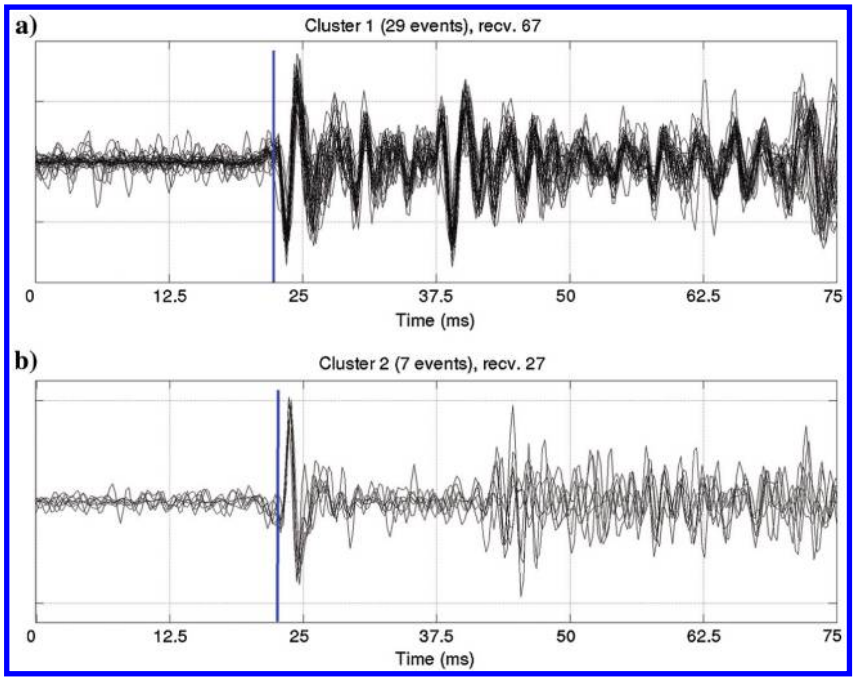

Figure 8. (a) P-wave coda waveforms in the radial component of a geophone in well G1 for the 29 strong microseismic events in cluster 1 aligned by waveform crosscorrelation and (b) aligned P-wave coda waveforms in the radial component at a geophone in well G3 for the seven events in cluster 2. The blue line indicates the onsets of the P-arrivals. The geometry is shown in Figure 2.

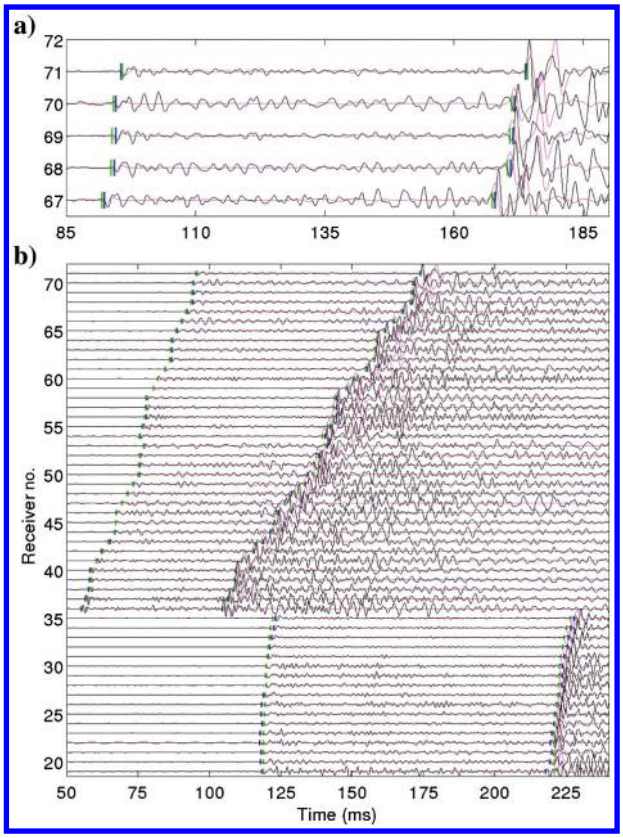

Figure 9. Comparisons between modeled and observed waveforms (b) and enlarged view of a few traces (a) for a typical event from cluster 1. The black traces are the observed waveforms, and the colored traces (magenta) are the modeled ones; the blue markers are the picked P- and SH-wave traveltimes, and the green ones are the modeled P- and SH-wave traveltimes. Traces from the north components in wells G3, G2, and G1 are shown from bottom up.

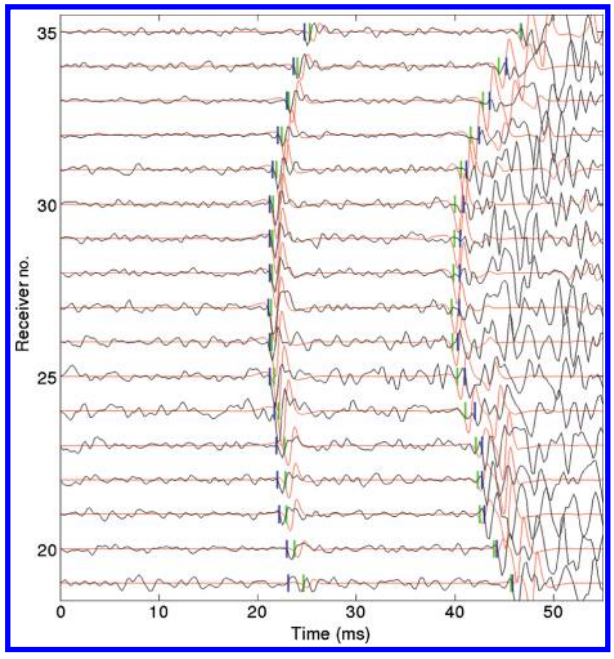

Figure 10. Comparisons between modeled and observed waveforms for a typical event from cluster two. The legends are the same as in Figure 9. Traces from the east components of well G3 are shown.

shows the P-waveform comparisons for the seven relatively smaller events from cluster 2 at a receiver in well G3. The events in this cluster are spread more than the events in the cluster 1, so their waveform coherence is weaker.

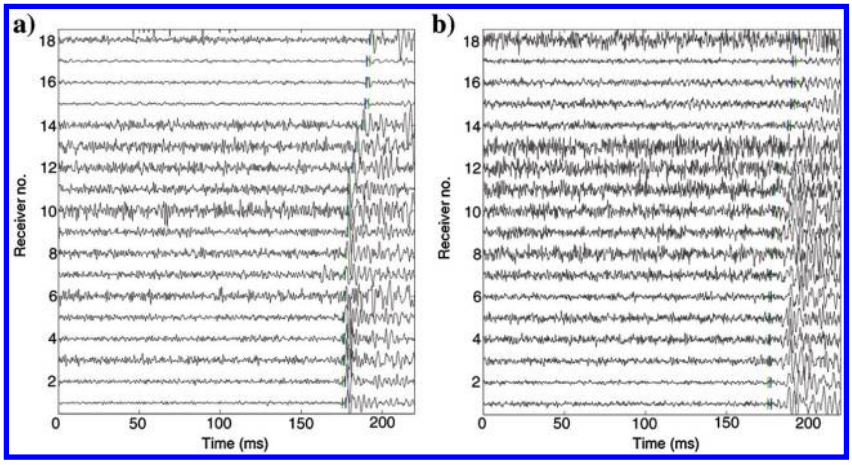

Figure 11. The same event from cluster 2 as shown in Figure 10, observed in one of the horizontal components (a) and in the vertical components (b) of the distant well G4. The blue and green markers are the picked and modeled SH-wave traveltimes in the horizontal components, respectively. The SV-arrivals can be clearly observed approximately 10 ms delayed after the SH-wave arrivals, especially at the first few geophones, due to the S-wave splitting. Note in this well P-wave arrivals are not picked and not used due to low S/N.

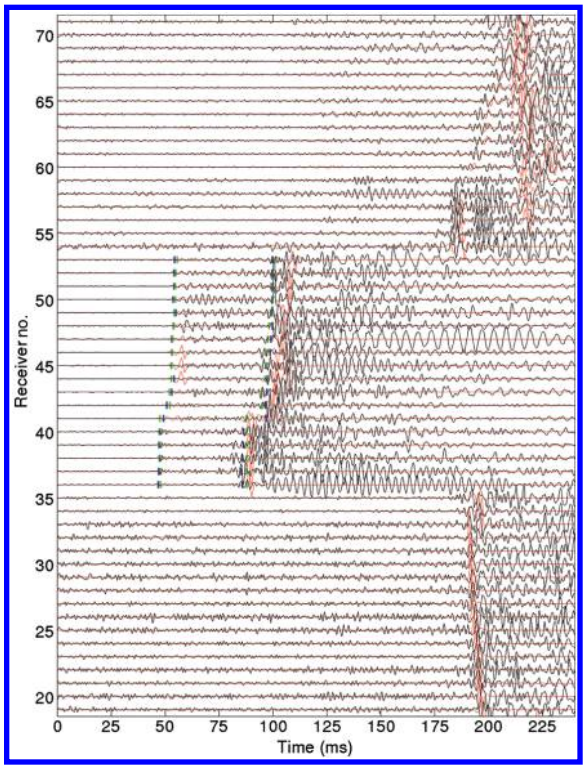

Figure 12. Comparisons between modeled and observed waveforms for a typical event from the Bakken. The markers are the same as in Figure 9. Traces in the east components of wells G1, G2, and G3 are shown.

We also found that all 68 selected strong events only come from the Bakken or the overlying Lodgepole formations. None of the events selected by S/N come from the Three Forks formation under the Bakken. This is consistent with two other observations. One is that, in some cases, excess produced water in hydraulically stimulated Bakken wells seems to be coming from the water-bearing interval with high permeability in the overlying Lodgepole formation above the Bakken when aggressive treatment parameters are used or when the overlying shale formation fails to vertically contain the fracture propagation (Hassen et al., 2012). The other observation is that cores from the Lodgepole exhibit large vertical fractures (V. Grechka, personal communication, 2013). We infer that hydraulic stimulation has activated preexisting fractures or faults, thereby creating a conduit up to the water-bearing upper interval and causing clustering of some of the larger microseisms along those fractures or faults. Given this explanation, we expect the occurrence of natural fractures or faults above the Middle Bakken affects the fracturing in the target interval.

Waveform comparison

We also validate our location and velocity inversion results by generating synthetic waveforms and comparing them with observed ones. The synthetic waveforms are calculated by our in-house finite-difference code that can handle heterogeneous media with up to orthorhombic anisotropy. The source properties used in generating the synthetic waveforms are manually estimated from the observed P- and SH-wave amplitudes and polarities, and the source wavelet is a smooth ramp with frequency contents similar with the observed waveforms (Bouchon, 2003; Li et al., 2011). Figure 9 shows the waveform comparison for a typical event from cluster 1 (see Figure 2 for geometry). With the final inverted anisotropic velocity model and determined hypocenters, we find not only good agreement between the modeled and observed traveltimes, but also between modeled and observed waveforms.

Figure 10 shows a typical event from cluster two, observed by the nearest well G3 (see Figure 2). This event is located in the Upper Lodgepole layer. The ray dip angles (measured from the vertical direction looking down) vary from approximately 40°–140° for this event, and within this range the wave speed changes considerably due to the anisotropies of the Upper as well as the Lower Lodgepole formations, which host this monitoring well. Still, we found that our two-layer anisotropic model for the Lodgepole formation characterizes the arrival moveout well.

The SH- and SV-arrivals of this event from cluster 2 are also observed in the distant well G4. Figure 11 shows considerable observed S-wave splitting due to VTI anisotropy for this event in well G4. The SV-arrivals in the vertical components (Figure 11b), which are shown with black traces, are significantly delayed compared with the SH-arrivals in the horizontal components (Figure 11a). It is found that the delay times between SH- and SV-waves are approximately 10 ms, while the total traveltimes are approximately 180 ms for the first few receivers in the near horizontal direction

in well G4. The magnitude of the traveltime delay means the SH-waves are approximately 6% faster than the SV-waves in the horizontal direction, consistent with our determined S-wave anisotropy of approximately 7% ($\gamma \approx 0.07$) for the Upper Lodgepole formation from the velocity inversion.

Figures 12 and 13 show the waveform and traveltime comparisons for a typical event from the Bakken formation. Due to the fine layering, very strong anisotropy and high-velocity contrast between the Bakken members, the observed waveforms become complex and thus it is hard to pick the traveltimes in distant wells. As a result, we only use traveltime picks from the nearest well G2 for location and velocity inversion for this event. Still, with the final location and joint anisotropic velocity inversion results, we generate synthetic waveforms in wells G1, G2, and G3 and find good agreement between the synthetic and observed waveforms in all these wells. For instance, in the distant well G3, the SH-phases and their move-out across the receivers are well matched between the observed and synthetic ones (Figure 12); in well G1, the observed waveforms are matched well with synthetic waveforms, even for receivers in the complex Bakken formation (Figure 13). Note in wells G1 and G3 the P-waves are difficult to observe, and the distinguishable matched phases are S-waves.

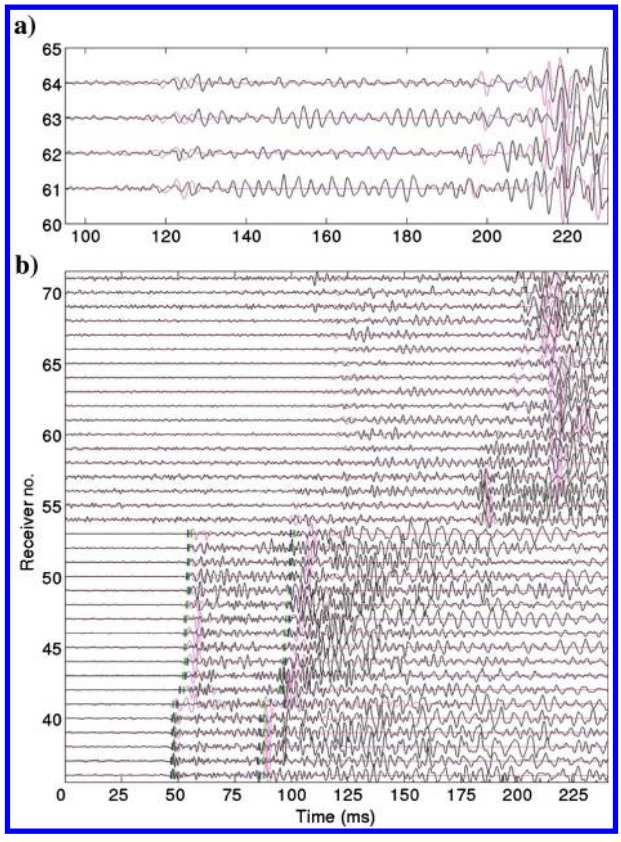

Figure 13. Same as Figure 12, but traces in the north components of wells G1 and G2 are shown. The panel (a) shows the close-up of a few typical traces from receivers within the Bakken formation in well G1 and the panel (b) shows all traces in wells G1 and G2. In some traces, the synthetic P-arrival phases are misaligned with observed ones by half a cycle, or 1–2 ms (compared with more than 100 ms traveltimes of the P-waves) due to slight inaccuracy in the velocity model or minor local velocity heterogeneity.

CONCLUSIONS

In this paper, we present our results locating 68 relatively strong microseismic events from the Bakken and its adjacent formations in the Beaver Lodge area of North Dakota using double-difference constraints and simultaneous anisotropic velocity inversion. We found that a six-layer simple model with VTI anisotropy can characterize quite well the information observed by four monitoring wells separated by up to 1500 m. The simultaneous anisotropic velocity inversion significantly reduces the traveltime residuals compared with standard location techniques. In general, we found very strong anisotropy in the shale members of the Bakken formation. The adjacent formations, consisting mainly of mudstones or siltstones, are also moderately anisotropic. However, not all elastic moduli or derived Thomsen's parameters in different layers were determined with equal certainty. The uncertainty analysis found that the traveltime has relatively low sensitivities with respect to the density normalized elastic moduli C_{13} and C_{33} in most layers due to limited ray coverage (Appendix A). Thus, the relative uncertainty in anisotropy parameter δ, which involves C_{13} and C_{33}, is larger than other anisotropy parameters.

Synthetic waveforms were also generated using the inverted hypocenters and the anisotropic velocity model. We compared the synthetic waveforms with the observed ones to verify our results based on the high-frequency ray approximation, finding satisfactory agreement. Waveform matching of some complex phases beyond first arrivals further validates our results. The match is satisfactory even at receivers not used for locating these events.

Swarms of strong events are found to occur repeatedly in the Lodgepole formation, high above the treatment well. Waveforms from the clustered events show strong similarities, indicating that the locations and source properties of these events are very close and suggesting reactivation of preexisting Lodgepole fractures, likely through some water-bearing fault or fracture conduits. It may be possible to optimize completion parameters in areas where these fractures exist if we can recognize them. Certainly, by properly locating events, microseismic monitoring is a valuable tool for detecting hydraulic fractures growing out of the designed zone and helps engineers properly evaluate fracture height growth and estimate the effectively SRV.

ACKNOWLEDGEMENTS

We thank Hess Corporation for access to the data set and for permission to publish this paper. We also thank Shell Oil Company for providing financial support for J. Li. M. van der Baan, and three anonymous reviewers gave very constructive comments to improve this paper.

APPENDIX A

VELOCITY INVERSION UNCERTAINTY ANALYSIS

In this section, we present the velocity inversion uncertainty analysis in the inverted density normalized elastic moduli C_{ij}. We perform a bootstrap test for each C_{ij} by randomly perturbing the determined value 100 times with a standard deviation equal to 5% of the value. Given a certain perturbation on an elastic modulus, the larger the resulting traveltime change, the larger the sensitivity

of the traveltime with respect to that parameter. Thus, the parameter can be determined more reliably. In general, we find perturbations on C_{11} and C_{66} for any layer result in relatively larger changes in traveltime than perturbations on other parameters do in the same layer, i.e., these two parameters for each layer are better determined relatively. In contrast, the traveltime changes caused by perturbation on C_{13} and C_{33} are usually less than 0.5%, except C_{13} in the Upper Lodgepole, suggesting these parameters are usually determined with appreciable uncertainty. The uncertainty for the parameter C_{55} is moderate.

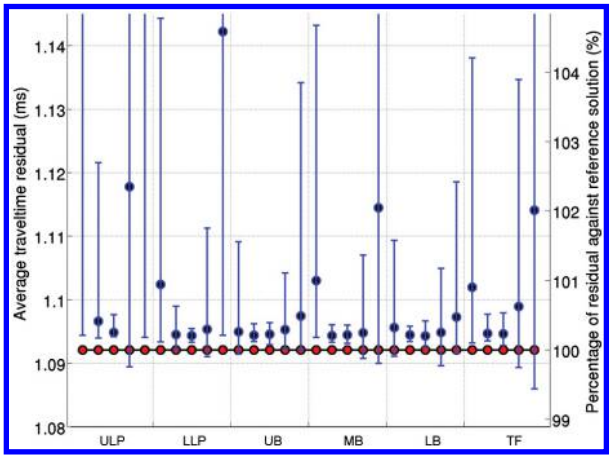

Figure A-1. Bootstrap test of the parameter sensitivities: ULP and LLP stand for the Upper and Lower Lodgepole formations, respectively; UB, MB, and LB stand for the Upper, Middle, and Lower Bakken formations, respectively; and TF stands for the Three Forks formation. The parameters for each layer are C_{11}, C_{13}, C_{33}, C_{55}, and C_{66} in sequence. The red dots indicate the traveltime residual (ms) of the reference solution with our regularized inversion. The bars indicate the range of the average traveltime residuals for the 100 random tests. The blue dots indicate the mean values. Note that the mean values for C_{11} and C_{66} in ULP are out of the range shown.

For each elastic modulus, the bar in Figure A-1 shows the range of the average traveltime residuals for the 100 random tests, and the blue dots show the mean values of these 100 average residuals. As most rays spend significant time traveling in the Upper Lodgepole formation, perturbations of elastic moduli of this layer cause larger changes in the average traveltime residual, especially perturbations on C_{11} and C_{66}, which characterize the horizontal P- and S-wave velocities, respectively (the ray angle coverages are shown in Figures A-2 and A-3). It should be noted sometimes the perturbation of certain elastic moduli can lead to small reduction in the traveltime residuals. This is because constraints on Thomsen's parameters are imposed in our inversion, thus elastic moduli attempting to retain predetermined Thomsen's parameters do not necessarily yield the minimum traveltime residuals.

We further show why the traveltime is more sensitive to some density normalized elastic moduli than others in a certain layer in Figures A-2 and A-3. Figure A-2 shows the group velocity sensitivity ($\partial v_g/\partial C_{ij}$, bolded lines) and ray count (gray bins) with group angles for P-waves in each layer. For a parameter in a certain layer, the more frequently the angles with higher sensitivity are sampled by rays, the less uncertainty the parameter has in the inversion. For instance, most P-rays travel beyond 60° in the Upper Lodgepole formation, and C_{11} has sensitivity increasing with angle, larger than any other P-wave related parameter beyond 70°, thus C_{11} is relatively better constrained than the other parameters in this layer; also, C_{33} has sensitivity decreasing with angle, smaller than any other parameter beyond 50°, thus C_{33} is more poorly constrained than the other P-wave related parameters in this layer. It should be noted that both the P- and SH-waves are sensitive to C_{55}, although for P-waves the largest sensitivity is at approximately 45°, and for SH-waves it is in the vertical direction (0°). In general, few rays are found at less than 40° in any layer, and, therefore, the determination of C_{33} in all layers is subject to noticeable uncertainty. As a result, the inverted Thomsen's ϵ would come with unavoidable uncertainty and constraints on these parameters with predetermined values are necessary in the inversion. Also, we found the sensitivity with respect to C_{55} is always larger than C_{13}, indicating the uncertainty in C_{55} should be smaller than in C_{13} comparatively.

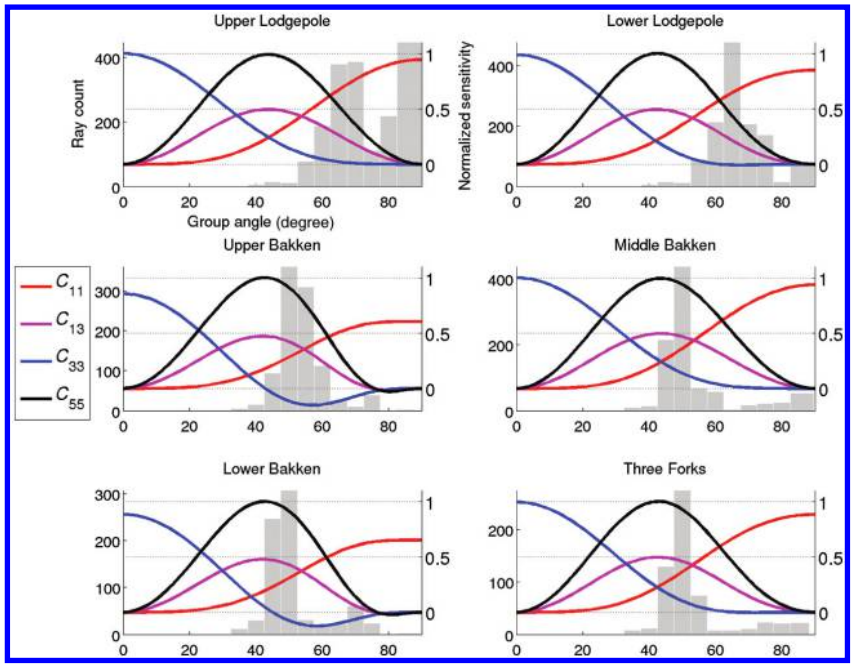

Figure A-2. Group velocity sensitivity (bold lines) and ray count (gray bins) with angle for P-waves in each layer. The sensitivities for each layer are normalized to the maximum sensitivity of all elastic moduli of that layer. Zero degrees is the vertical direction, and 90° is the horizontal direction.

Figure A-3 shows the group velocity sensitivity and ray count with group angles for SH-waves in each layer. Similar to P-waves, most incident rays are at high angles. For SH-waves, when the group angle is larger than 50°, the group velocity sensitivity with respect to C_{66} is larger than with respect to C_{55} in all layers. Still, as mentioned above P-waves can also help to determine C_{55}. Judging from the sensitivities and the resulting traveltime changes with perturbation on C_{55}

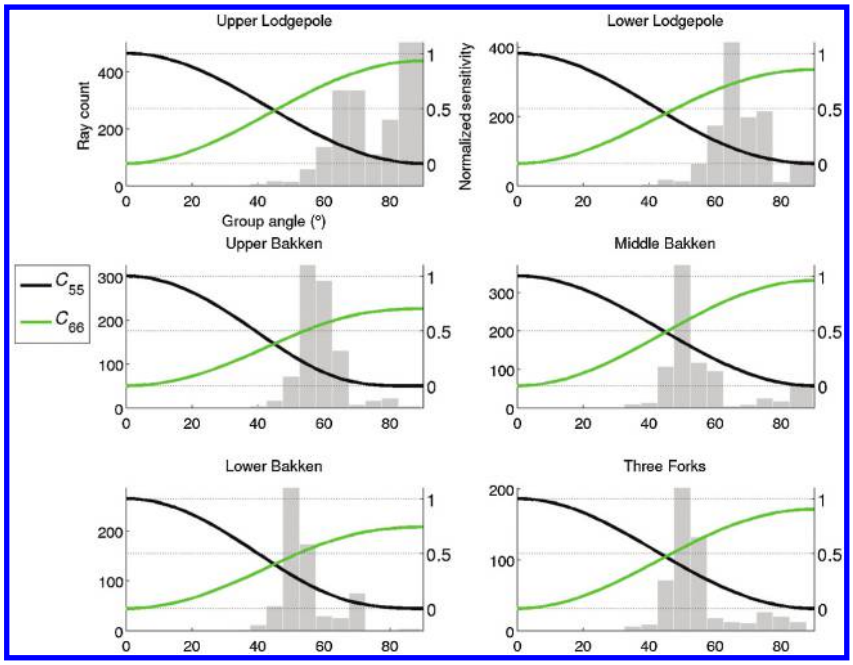

Figure A-3. Group velocity sensitivity (bold lines) and ray count (gray bins) with angle for SH-waves in each layer.

and C_{66} (Figure A-1), Parameter γ should be inverted with less uncertainty compared with ϵ, which involves one of the least constrained parameter C_{33}. Also, the uncertainty in parameter δ, which involves C_{13} and C_{33}, is also determined with more uncertainty than with ϵ.

REFERENCES

Bai, C. Y., G. J. Huang, X. L. Li, B. Zhou, and S. A. Greenhalgh, 2013, Ray tracing of multiple transmitted/reflected/converted waves in 2D/3D layered anisotropic TTI media and application to crosswell traveltime tomography: Geophysical Journal International, **195**, 1068–1087, doi: 10.1093/gji/ggt267.

Bouchon, M., 2003, A review of discrete wavenumber method: Pure and Applied Geophysics, **160**, 445–465, doi: 10.1007/PL00012545.

Castellanos, F., and M. Van der Baan, 2013, Microseismic event locations using the double-difference algorithm: CSEG Recorder, **38**, 26–37.

Dreger, D., R. Uhrhammer, M. Pasyanos, J. Franck, and B. Romanowicz, 1998, Regional and far-regional earthquake locations and source parameters using sparse broadband networks: A test on the Ridgecrest sequence: Bulletin of the Seismological Society of America, **88**, 1353–1362.

Grechka, V., P. Singh, and I. Das, 2011, Estimation of effective anisotropy simultaneously with locations of microseismic events: Geophysics, **76**, no. 6, WC143–WC155, doi: 10.1190/geo2010-0409.1.

Hassen, B., Y. Zotskine, and D. Gulewicz, 2012, Hydraulic fracture containment in the Bakken with a synthetic polymer water based fracture fluid: Presented at Society of Petroleum Engineers Canadian Unconventional Resources Conference paper , 162670.

Havens, J., 2012, Mechanical properties of the Bakken formation: M.S. thesis, Colorado School of Mines.

Hayles, K., R. L. Horine, S. Checkles, and J. P. Blangy, 2011, Comparison of microseismic results from the Bakken Formation processed by three different companies: Integration with surface seismic and pumping data: 81st Annual International Meeting, SEG, Expanded Abstracts, 1468–1472.

Horne, S., 2013, A statistical review of mudrock elastic anisotropy: Geophysical Prospecting, **61**, 817–826, doi: 10.1111/1365-2478.12036.

Huang, C., C. Y. Bai, D. L. Zhu, and S. A. Greenhalgh, 2012, 2D/3D seismic simultaneous inversion for the velocity model and interface geometry using multiple classes of arrivals: Bulletin of the Seismological Society of America, **102**, 790–801, doi: 10.1785/0120110155.

Kocon, K., and M. Van der Baan, 2012, Quality assessment of microseismic event locations and traveltime picks using a multiplet analysis: The Leading Edge, **31**, 1330–1337, doi: 10.1190/tle31111330.1.

Levenberg, K., 1944, A method for the solution of certain non-linear problems in least squares: Quarterly of Applied Mathematics, **2**, 164–168.

Li, C., T. Dohmen, S. Morton, K. Katahara, K. Hayles, S. Checkles, and J. P. Blangy, 2012a, Evaluating the quality of microseismic event locations: 82nd Annual International Meeting, SEG, Expanded Abstracts, doi: 10.1190/segam2012-1155.1.

Li, J., H. Zhang, H. S. Kuleli, and M. N. Toksoz, 2011, Focal mechanism determination using high-frequency waveform matching and its application to small magnitude induced earthquakes: Geophysical Journal International, **184**, 1261–1274, doi: 10.1111/j.1365-246X.2010.04903.x.

Li, J., H. Zhang, W. L. Rodi, and M. N. Toksöz, 2012b, Joint microseismic location and anisotropic tomography using differential arrival times and differential back azimuths: 82nd Annual International Meeting, SEG, Expanded Abstracts, doi: 10.1190/segam2012-1382.1.

Li, J., H. Zhang, W. L. Rodi, and M. N. Toksöz, 2013, Joint microseismic location and anisotropic tomography using differential arrival times and differential back azimuths: Geophysical Journal International, **195**, 1917–1931, doi: 10.1093/gji/ggt358.

Magotra, N., N. Ahmed, and E. Chael, 1989, Single-station seismic event detection and location: IEEE Transactions on Geoscience and Remote Sensing, **27**, 15–23, doi: 10.1109/36.20270.

Maxwell, S. C., J. Rutledge, R. Jones, and M. Fehler, 2010, Petroleum reservoir characterization using downhole microseismic monitoring: Geophysics, **75**, no. 5, A129–A137, doi: 10.1190/1.3477966.

Meissner, F. F., 1991, Petroleum geology of the Bakken Formation Williston Basin, North Dakota, and Montana: Presented at Montana Geological Society 24th Annual Conference.

Rutledge, J. T., and W. S. Phillips, 2003, Hydraulic stimulation of natural fractures as revealed by induced microearthquakes, Carthage Cotton Valley gas field, east Texas: Geophysics, **68**, 441–452, doi: 10.1190/1.1567214.

Tang, W., and L. Li, 2008, Exact traveltime computation in multi-layered transversely isotropic media with vertical symmetry axis: Acta Seismologica Sinica, **21**, 370–379, doi: 10.1007/s11589-008-0370-6.

Tang, X., 2003, Determining formation shear-wave transverse isotropy from borehole Stoneley-wave measurements: Geophysics, **68**, 118–126, doi: 10.1190/1.1543199.

Thomsen, L., 1986, Weak elastic anisotropy: Geophysics, **51**, 1954–1966, doi: 10.1190/1.1442051.

Vernik, L., and X. Liu, 1997, Velocity anisotropy in shales: A petrophysical study: Geophysics, **62**, 521–532, doi: 10.1190/1.1444162.

Waldhauser, F., and W. L. Ellsworth, 2000, A double-difference earthquake location algorithm: Method and application to the northern Hayward fault, California: Bulletin of the Seismological Society of America, **90**, 1353–1368, doi: 10.1785/0120000006.

Walsh, J., B. Sinha, T. Plona, D. Miller, and D. Bentley, 2007, Derivation of anisotropy parameters in a shale using borehole sonic data: 77th Annual International Meeting, SEG, Expanded Abstracts, 323–326.

Warpinski, N. R., M. J. Mayerhofer, M. C. Vincent, C. L. Cipolla, and E. R. Lolon, 2008, Stimulating unconventional reservoirs: Maximizing network growth while optimizing fracture conductivity: Presented at Society of Petroleum Engineers Unconventional Reservoirs Conference, Paper 114173.

Warpinski, N. R., C. K. Waltman, J. Du, and Q. Ma, 2009, Anisotropy effects in microseismic monitoring: Presented at Society of Petroleum Engineers Annual Technical Conference and Exhibition, Paper 124208.

Warpinski, N. R., R. B. Sullivan, J. E. Uhl, C. K. Waltman, and S. R. Machovoie, 2005, Improved microseismic fracture mapping using perforation timing measurements for velocity calibration: SPE Journal, **10**, 14–23, doi: 10.2118/84488-PA.

Wolfe, C. J., 2002, On the mathematics of using difference operators to relocate earthquakes: Bulletin of the Seismological Society of America, **92**, 2879–2892, doi: 10.1785/0120010189.

Zhang, H., and C. H. Thurber, 2003, Double-difference tomography: The method and its application to the Hayward Fault, California: Bulletin of the Seismological Society of America, **93**, 1875–1889.

Zhang, H. J., S. Sarkar, M. N. Toksoz, S. Kuleli, and F. Al-Kindy, 2009, Passive seismic tomography using induced seismicity at a petroleum field in Oman: Geophysics, **74**, no. 6, WCB57–WCB69, doi: 10.1190/1.3253059.

Zhang, H. J., and C. H. Thurber, 2006, Development and applications of double-difference seismic tomography: Pure and Applied Geophysics, **163**, 373–403, doi: 10.1007/s00024-005-0021-y.

Zhou, B., and S. A. Greenhalgh, 2005a, Analytic expressions for the velocity sensitivity to the elastic moduli for the most general anisotropic media: Geophysical Prospecting, **53**, 619–641, doi: 10.1111/j.1365-2478.2005.00490.x.

Zhou, B., and S. Greenhalgh, 2005b, Shortest path ray tracing for the most general 2D/3D anisotropic media: Journal of Geophysics and Engineering, **2**, 54–63, doi: 10.1088/1742-2132/2/1/008.

Zhou, B., and S. A. Greenhalgh, 2006, Raypath and traveltime computations for 2D transversely isotropic media with dipping symmetry axes: Exploration Geophysics, **37**, 150–159.

Zhou, B., and S. A. Greenhalgh, 2008, Velocity sensitivity of seismic body waves to the anisotropic parameters of a TTI medium: Journal of Geophysics and Engineering, **5**, 245–255, doi: 10.1088/1742-2132/5/3/001.

Zhou, B., S. A. Greenhalgh, and A. Green, 2008, Nonlinear traveltime inversion scheme for crosshole seismic tomography in tilted transversely isotropic media: Geophysics, **73**, no. 4, D17–D33, doi: 10.1190/1.2910827.